Results in Engineering 17 (2023) 100921

Contents lists available at ScienceDirect

Results in Engineering

journal homepage: www.sciencedirect.com/journal/results-in-engineering

Optimizing the morphology of titania nanorods for enhanced solar seawater splitting

Paweł Wyżga [a], Taymaz Tabari [b,**], Mateusz Trochowski [b], Wojciech Macyk [a,b,*]

[a] InPhoCat – Innovative Photocatalytic Solutions Sp. z o.o., ul. Brzask 49, 30-381 Kraków, Poland
[b] Faculty of Chemistry, Jagiellonian University, ul. Gronostajowa 2, 30-387 Kraków, Poland

ARTICLE INFO

Keywords:
Solar water splitting
Hydrogen production
TiO_2 nanorods
Morphology control
Photoanode

ABSTRACT

Nanorod-TiO_2 electrodes were obtained by a hydrothermal method in the presence of different concentrations of sodium chloride. The addition of NaCl during the synthesis promoted the formation of thinner, well-crystallized nanorods growing along the [001] crystallographic direction, while still, the most intense reflection is related to (101). The optimal electrode demonstrated applied bias photon to current efficiency (ABPE) of 0.24% in solar seawater splitting, which is among the highest reported efficiencies for the pristine TiO_2 nanorods. Noteworthy, the ABPE of the obtained electrodes stayed intact during variation of the solar irradiation in the range of 0.2–1 Sun. It was also demonstrated that the efficiency of nanorod-TiO_2 electrodes is higher for seawater splitting (0.5 M NaCl) than for water photoelectrolysis in the presence of 0.5 M Na_2SO_4. This phenomenon is the result of chloride evolution reaction taking place in addition to water oxidation. A gradual decrease in efficiency resulting from the low mobility of holes was observed for all electrodes. This conclusion was confirmed by experiments with a hole-scavenger (improved performance of the cell), as well as surface photovoltage measurements and electrochemical impedance spectroscopy.

1. Introduction

Global energy consumption is constantly growing and is predicted to increase by 50% between 2010 and 2050 [1,2]. In this context, green energy is one of the key elements of sustainable development [3,4] and is an important means to achieve the objectives of the 2015 Paris Agreement [5]. Solar, wind, and nuclear power plants are among the possible clean energy sources with low CO_2 emissions [6–8]. The recent development of photovoltaic cells increased the hope for more efficient exploitation of solar energy [9–12]. However, storing solar energy to allow its transportation is an equally important task [13,14]. Among the possible technologies, solar water splitting enables storing the energy of light in the hydrogen bond, which is a clean, transportable, and cost-effective energy source [15,16]. Water splitting is an uphill reaction, which needs 237 kJ to produce 1 mol of hydrogen [17]. To provide it, solar energy can be used to oxidize/reduce water. However, using freshwater as an electrolyte for water splitting is expensive due to the cost of the purification process. At the same time, more than 96% of the available water is sea/ocean water, which makes it a perfect feed for solar water splitting due to its abundance and natural conductivity [18,19]. In seawater oxidation, the oxygen evolution reaction (OER) can be partially or fully replaced by the chlorine evolution reaction (ClER). In the early work of Bennett, it was shown that ClER is the main route in direct seawater oxidation, whereas OER exists at current densities below 1 mA cm^{-2} or at extremely high current densities where the mass transfer prevents the ClER to proceed [20]. Moreover, Dionigi et al. determined the potential and pH ranges in which ClER is highly competitive with OER [21]. The PV-integrated electrocatalytic (EC) system, reported by Hsu et al., showed high solar to hydrogen efficiency with no trace of chlorine production, while for the catalysts with lower activity, production of Cl_2 was recorded [22], corroborating Bennett's report. In the genuine photoelectrochemical (PEC) systems reported by Rassoolkhani et al., the ClER was detected upon an applied potential of 1.6 V *vs.* RHE, which was higher than the thermodynamic potential (1.42 V *vs.* RHE) of $Cl_2/2Cl^-$ redox couple, facilitating 80% of oxidation processes to proceed as ClER. Moreover, Jadwiszczak et al. [23]. Reported chlorine production under lower potentials compared to the thermodynamic potential of the $Cl_2/2Cl^-$ redox couple and observed a low Faradaic efficiency and stability during their measurements. However, the current density was higher than 1 mA cm^{-2}, again correlating

* Corresponding author. Faculty of Chemistry, Jagiellonian University, ul. Gronostajowa 2, 30-387 Kraków, Poland.
** Corresponding author.
E-mail addresses: taymaz.tabari@uj.edu.pl (T. Tabari), macyk@chemia.uj.edu.pl (W. Macyk).

https://doi.org/10.1016/j.rineng.2023.100921
Received 5 October 2022; Received in revised form 15 January 2023; Accepted 26 January 2023
Available online 2 February 2023

with Bennett's results.

Solar water splitting can be realized by employing particle semiconductors. However, the efficiency of such systems is low because of the increased charge recombination rate [24,25]. Interestingly, the lifetime of the photoinduced charge carriers can be enhanced by using structurally designed 1D semiconductors [26–28]. As a result of anisotropic crystal morphology, they are characterized by a directional charge transfer, which facilitates charge separation. In photoanode, for example, positive charge carriers travel to the electrode/electrolyte interface, while the negative charge carriers migrate to the counter electrode. There is a tremendous number of reports on rod architecture design and engineering with a focus on controlling the thickness of the film, which strongly influences the absorption coefficient and overall activity of the electrodes [29–33]. At the same time, controlling the length and thickness of the rods *via* applying the well-known hydrothermal synthesis methods, seems to be a challenging task. This is directly related to the crystallization process of the rods, in which the rod size is an outcome of a competition between nucleation and crystal growth stages [32,34]. If nucleation is faster than crystal growth, the diameter of the rod is thinner, and *vice versa* [35]. In the synthesis of metal oxide rods, such as TiO_2 and Fe_2O_3, the whole process of determining the thickness and length is controlled by pH, temperature, and time [29,34].

NaCl is an environmentally benign and cost-effective salt, which can be employed to increase the ionicity of the solution without increasing the acidity. In other words, by adding the NaCl to the solution, the concentration of positive and negative charges (Na^+ and Cl^-) will be increased without changing the pH. Moreover, NaCl is an active catalyst in oxidation and decoupling processes [36,37]. These properties encouraged researchers to use NaCl during the synthesis process. Previously, Liu et al. employed a series of surfactants and salts, including NaCl, to synthesize nanorod-TiO_2, which was used in an integrated dye-sensitized solar cell [29]. Their finding shows that in presence of a concentrated solution of NaCl, both the diameter and density of the rods are decreased, resulting in less active nanorod TiO_2. However, they were unable to define the role of NaCl in this matter. Next, Rui et al. showed that in the presence of NaCl, rutile is the major product of the synthesis [30]. However, they were unable to control the shape and size of the rods, and instead of achieving a uniform film, they synthesized an urchin-shaped structure. In those publications, the role of NaCl was attributed to the increased ionic strength of the solution.

In this comprehensive study, uniform films of TiO_2 nanorods were synthesized with the use of NaCl, and their activity in water and synthetic seawater splitting was tested under different intensities of the LED and simulated solar light. We show, that the application of relatively simple approaches to the synthesis of TiO_2 nanorods and the use of seawater as an electrolyte can result in photoelectrodes of significant performance, comparable to those observed in the case of much more sophisticated TiO_2-based heterostructural architectures.

2. Material and methods

2.1. Synthesis of TiO_2 nanorods

A hydrothermal process was used for the synthesis of the nanorod-TiO_2 electrodes. Twelve series of materials were prepared using different concentrations of NaCl and calcination temperatures. The control samples (without NaCl) were synthesized in a solution consisting of deionized water (DI water), titanium isopropoxide (97%, Sigma Aldrich), and concentrated HCl (37%, Sigma Aldrich) in a volume ratio of 12:0.35:12 ml, respectively, whereas for the other series 1 ml of NaCl (pure, Carl Roth) solution (1, 2, and 3 M) was additionally added to the given mixture with volume ratios 11:0.35:12 ml. Synthesis solutions were placed in the Teflon-lined stainless-steel autoclave and kept at 150 °C for 12 h. After the process, the samples were thoroughly washed with DI water to remove any excess NaCl from the surface. Then, the electrodes were treated for 15 min in a Diener low-pressure oxygen plasma generator to remove organic residue left on the surface. Next, the electrodes were divided into groups and calcined under different temperatures: 300, 450, and 600 °C. The heating/cooling rate and annealing time at the final temperature were 1 °C/min and 2 h, respectively. Evenly coated nanorod-TiO_2 layers covered a 1 cm^2 area of the obtained electrodes. To keep the text concise, the samples were labeled as NTX_YYY, where X stands for concentration of NaCl during synthesis and YYY is the calcination temperature, *e.g.*, NT1_300 (1 M NaCl, 300 °C).

2.2. Structural and physicochemical characterization of the electrodes

The structural and physicochemical properties of the prepared samples were studied using several techniques. The characterization methodology related to the X-ray diffraction (XRD), X-ray photoelectron spectroscopy (XPS), surface photovoltage (SPV), scanning electron microscope (SEM) and diffuse reflectance spectroscopy (UV–vis DRS) was similar to our previous work [26]. The least-square fit of the selected X-ray reflections was performed with WinCSD software [38]. The morphology in nanoscale was thoroughly investigated employing transmission electron microscopy (TEM) and selected area electron diffraction (SAED) using Tecnai TF 20 X-TWIN microscope (FEI, Hillsboro, USA; FEG, 200 kV). Samples for TEM analysis were scraped off the synthesized electrodes, dispersed in isopropanol using an ultrasonic bath, and transferred onto a copper grid. The bandgap energy of the materials was estimated using the modified Tauc plots [39]. Raman spectra were recorded under a green laser (532 nm) employing a Renishaw InVia spectrometer, which was equipped with a CCD detector and a Leica DMLM confocal microscope.

2.3. Photoelectrochemical characterization of the electrodes

Linear sweep voltammetry and chronoamperometry with LED light illumination were performed using Mini Photoelectric Spectrometer (*Instytut Fotonowy*) equipped with an LED revolver (371, 388, 397, 425, and 455 nm, spectra are given in Fig. S10). Experiments with simulated solar light were conducted using the xenon arc lamp (XBO, 150 W, *Instytut Fotonowy*, spectrum given in Fig. S11) equipped with the AM 1.5G filter and water filter. The absorption of the FTO glass substrate was taken into account during setting up the experiments. Measurements were conducted with a three-electrode setup in 0.5 M NaCl (pure, *Chempur*) and 0.5 M Na_2SO_4 (>99%, *Alfa Aesar*) using platinum wire and Ag/AgCl (3 M KCl, redox. me) as counter and reference electrodes, respectively. The selected samples were additionally tested in 0.5 M NaCl with the addition of 5%wt. of methanol (pure, *Warchem*) as a hole scavenger. The working electrode was irradiated from the backside. Before each test, the surface of the Pt electrode was cleaned by dipping it in concentrated sulfuric acid for 1 min and the electrolyte was purged with Ar for at least 30 min. Herein, according to the work of Chen et al., the Pt deposition on the working electrode during the water splitting reaction can be neglected, since Pt is prone to redeposition on the cathode and a slight dissolution of Pt cannot have an impact on the activity of the OER photocatalyst [40]. Applied potentials were normalized according to the reversible hydrogen electrode (RHE) using the Nernst equation (Eq. (1)):

$$V_{RHE}\ [mV] = V_{applied\ vs.\ Ag/AgCl} + 212\ mV + (59.2\ mV \times pH) \quad (1)$$

where 212 mV is the potential of Ag/AgCl (3 M KCl) versus standard hydrogen electrode.

Photocurrent density, j_{ph}, was obtained by subtracting current density values measured under illumination and in dark. The electrochemical impedance spectroscopy (EIS) was conducted under simulated solar irradiation (AM 1.5 G) with a frequency range from 100 kHz to 0.1 Hz in 0.5 M Na_2SO_4 (≥99%, Sigma Aldrich). The frequency response

analysis (FRA) potential scan is performed within the potential range of −500 to 1600 mV *vs.* RHE, while the frequency was ranging from 10 kHz to 0.1 Hz.

3. Results and discussion

3.1. Structural and physicochemical analysis

3.1.1. X-ray diffraction

The synthesized nanorod-TiO_2 films formed uniform, opaque layers on the FTO substrate. The X-ray diffraction (XRD) analysis revealed all obtained samples to contain exclusively rutile phase (space group $P4_2/mnm$, $a \approx 4.59$ Å, $c \approx 2.96$ Å), and the observed reflections were indexed with (101), (111), (002), (301), and (112) Miller indices (Fig. 1, Fig. S1). Additional peaks are related to the FTO substrate layer (JCPDS card number #77–452). In general, the (110) reflection (the most intensive one in the theoretical diffractogram for rutile) was absent in each XRD pattern and the intensities of the other peaks strongly differ from the theoretical ones (Fig. 1). This is a clear indication of the preferred orientation of the grown films. It was proposed previously that the addition of NaCl during the hydrothermal synthesis influences the morphology and growth direction of the films, due to the selective adsorption of chloride ions onto the (110) surface [30,41]. For NT0 samples synthesized without NaCl (Fig. 1a), the (101) reflection has the highest intensity, indicating the exposition of the (101) plane of nanorods. Moreover, in this series, the crystallinity is improved with increasing temperature. After the addition of 1 M NaCl, the (002) peak became the most intense one (intensity ratio $I_{(101)}/I_{(002)} = 0.3–0.5$, Table S1, Fig. 1b). Upon further increase of NaCl concentration, the intensity ratio $I_{(101)}/I_{(002)}$ again increased (1.1–1.3 and 1.8–3.1 within NT2 and NT3 series respectively, Table S1, Fig. 1c and d). This indicates the change of the most exposed crystallographic plane from (002) again to (101) upon increasing NaCl concentration from 1 M to 3 M. Since this may originate from an inclination of nanorods with respect to the substrate or a different crystallographic growth direction of nanorods, this observation will be verified with TEM analysis in the following part. Generally, the full width at half-maximum (FWHM) of the peaks decreased for the higher NaCl concentration, *e.g.*, from 0.38–0.42° to 0.25–0.26° for NT0 and NT3 series, respectively (Table S1), which suggests enhancement in the crystallinity and/or in the grain size of the nanorod-TiO_2 layer. Moreover, (111) and (301) peaks, not observed for the NT0_300 sample, appeared for NT2_300 and NT3_300, which proves that the presence of NaCl facilitates achieving higher crystallinity at a lower temperature. Interestingly, for the films annealed at 450 °C, the FWHM of the (101) and (002) reflections were lower than for samples calcined at 300 and 600 °C, which suggests a higher degree of crystallinity and/or larger diameter of rods in films calcined at 450 °C.

3.1.2. Raman spectroscopy

The Raman spectra of the nanorod-TiO_2 samples (Fig. 2) were in agreement with previously reported ones for the rutile phase [42]. Two first-order Raman peaks observed at 447, and 610 cm^{-1} can be

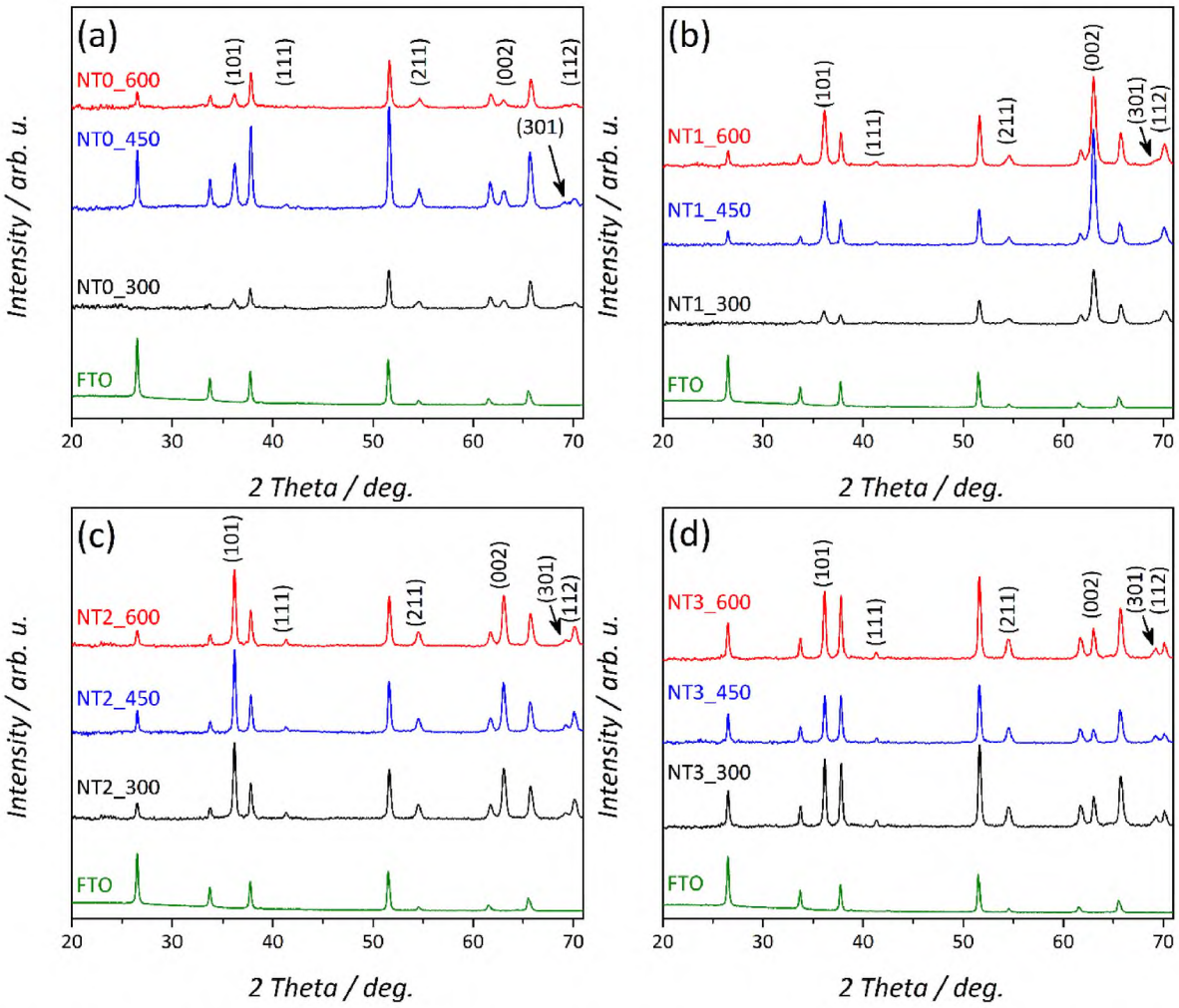

Fig. 1. XRD patterns of the synthesized nanorod-TiO_2 samples using different concentrations of NaCl and different calcination temperatures: 0 M NaCl (a), 1 M NaCl (b), 2 M NaCl (c), and 3 M NaCl (d).

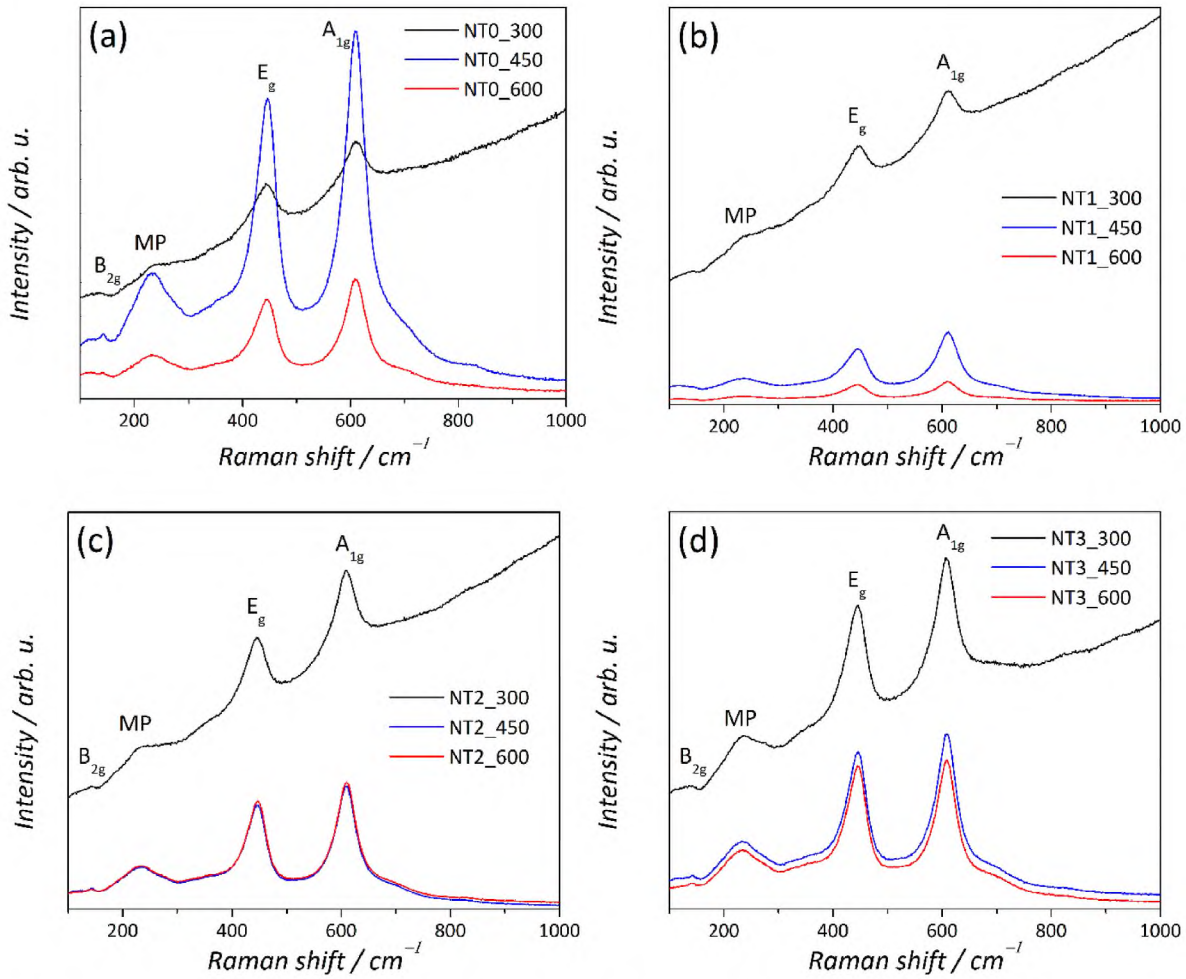

Fig. 2. Raman spectra of nanorod-TiO_2 prepared in different conditions: 0 M NaCl (a), 1 M NaCl (b), 2 M NaCl (c), and 3 M NaCl (d).

attributed to E_g, and A_{1g} modes, respectively. An additional peak related to the multiple phonon scattering (MP) Raman mode was observed at 240 cm^{-1} and it originates from the presence of small particles below 25 nm [43]. Moreover, the B_{2g} mode (143 cm^{-1}) was observed for the 2 M and 3 M series, as well as for the NT0_450 sample. The sloping background observed in spectra of samples calcined at 300 °C may result from the lower crystallinity of the nanorods (compare Fig. 1). Peak positions remained practically constant (within 1–3 cm^{-1}), without any systematic changes (Fig. 2). For instance, spectra of nanorod-TiO_2 samples annealed at 600 °C were compared in Fig. S3.

3.1.3. *X-ray photoelectron spectroscopy*

The X-ray photoelectron spectroscopy (XPS) results of the TiO_2 series are collected in Fig. S4. The XPS core-level analysis of Ti 2*p* of all samples revealed two intense peaks at 459 and 464 eV, characteristic of the rutile phase [44–46], which correspond to Ti $2p_{3/2}$ and Ti $2p_{1/2}$, respectively. The formal oxidation number of titanium is 4+. Shifts in peak positions between samples (<0.3 eV) were below the resolution limit of the used XPS apparatus. The signal originating from the O 1*s* core level, for all samples, appeared as two peaks, centered at 530 and 532 eV, which are attributed to the lattice oxygen (Ti–O) and adsorbed oxygen (O–H), respectively [44]. The ratio between these two peaks (I_{Ti-O}/I_{O-H}) was unchanged for samples within NT1 and NT3 series (Figs. S4d and h), whereas it was the lowest for samples calcined at 450 °C within NT0 and NT2 series. This suggests the higher content of the adsorbed oxygen for NT0_450 and NT2_450 samples compared with other specimens in the respective series. Generally, samples synthesized in the presence of NaCl (NT1-NT3) showed a higher I_{Ti-O}/I_{O-H} ratio, *i.e.*, a lower amount of the adsorbed oxygen, than respective specimens obtained without NaCl (NT0 series). O 1*s* core level analysis of the NT2 series showed an increased content of adsorbed oxygen compared to the lattice oxygen. In both NT1 and NT2 series, the content of lattice oxygen is significantly larger compared to the adsorbed oxygen. Notably, the ratio of the Ti–O/O–H in the NT3 series was smaller than in the NT1 series. It seems that at higher NaCl concentrations (2 and 3 M) the content of surface O–H groups increased.

3.2. *Morphology analysis*

The scanning electron microscopy (SEM) top-view images are shown in Fig. 3 and Fig. S6. The NT0_300 sample showed well-grown and uniform rods with sharp ends, while NT0_450 consists of uniform thick rods with flatter ends. NT0_600 imitated a similar morphology to NT0_300 with sharp ends. The flat-ended rods in the NT0_450 sample along with its thicker architecture point to the growth of different crystallographic planes compared to NT0_300 and NT0_600 architectures, which supports the conclusions from the XRD analysis. Moreover, NT1_300 revealed a similar morphology with thinner rod architecture compared to the NT0 series. The NT1_450 sample showed a lower uniformity of rods compared to NT1_300 and was constructed from considerably thinner rods (major structure) grown among thicker rods (minor structure). Such morphology generates several inter-rod connections that can have an impact on charge transportation and thus, its collection and recombination. NT1_600 indicated uniform, thin, and well-grown rod architecture, which is morphologically resembling NT1_300, being slightly thinner than that of NT1_300. All rods of the

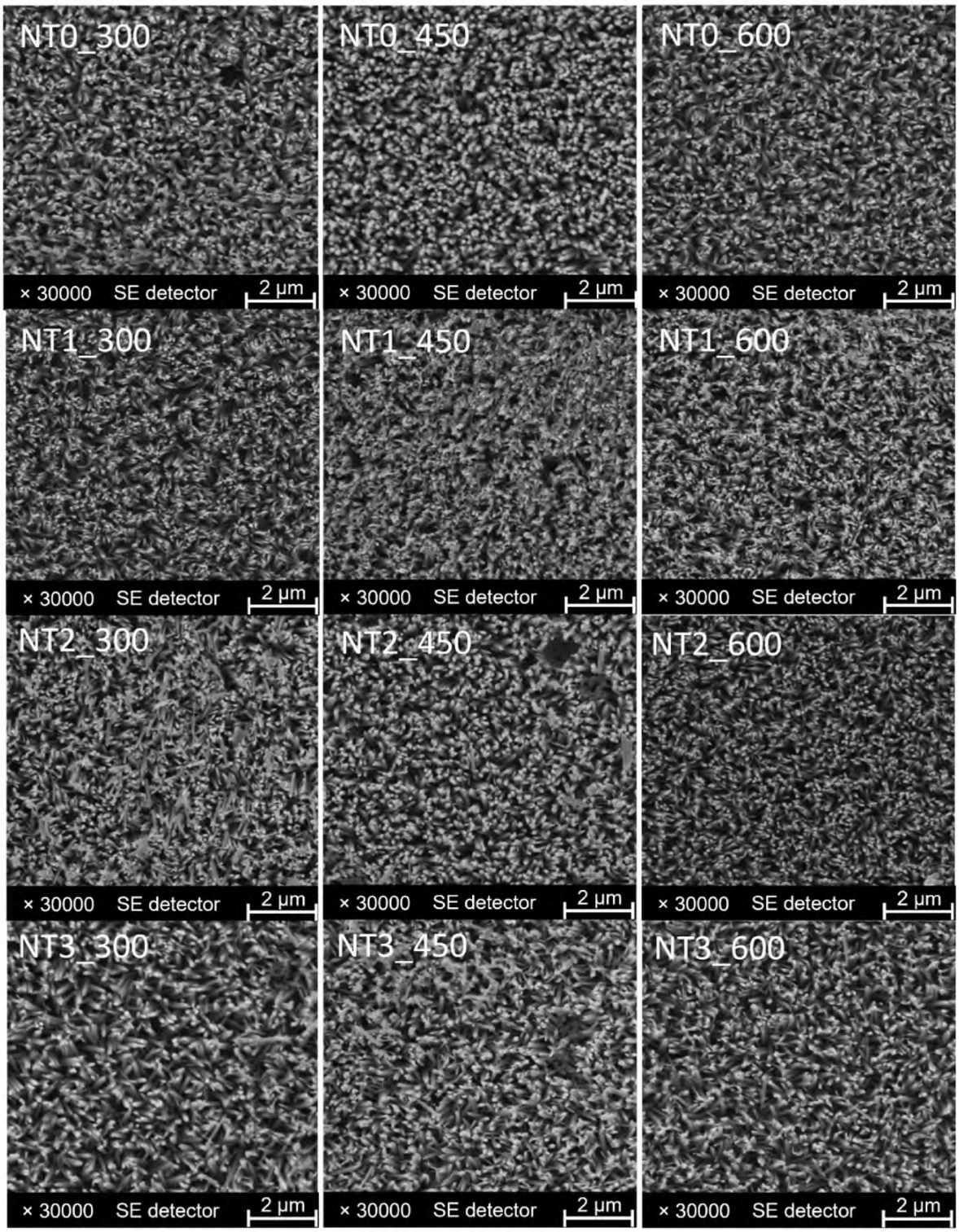

Fig. 3. The SEM micrographs of the nanorod-TiO_2 samples, synthesized under different conditions.

NT1 series are sharp-ended. NT2_300 demonstrated two different rod structures, in which some of the rods align horizontally on the vertically grown ones. NT2_450 shows flat-ended thick rod architecture, which has a more uniform structure with an insignificant number of rods grown horizontally compared to NT2_300. In addition, NT2_600 was characterized by uniform, well-constructed rods with sharper ends compared to NT2_300 and NT2_450. However, in general, the NT2 series demonstrated a more round-ended rod structure compared to NT0 and NT1 series. Furthermore, NT3_300 showed less sharp-ended, uniform rods. While NT3_450 clearly demonstrates two different types of rods, in which thin rods (as minor features) grow among the vertically aligned thick rods (major features). NT3_600 shows thin rods grown among the thicker rods. However, in general, the thickness of the rods in NT3_600 is increased compared to NT3_450. Also, in NT3_600, the smaller rods are stand-alone vertically, while in NT3_450, the thinner rods are laying on the thicker ones.

The cross-sections of the obtained electrodes are depicted in Fig. S7. The synthesized nanorod-TiO_2 formed uniform and dense layers with thicknesses ranging from 0.7 to 2.7 μm. In general, the addition of NaCl during the synthesis resulted in the increased layer thickness for each calcination temperature – the weakest relation was observed for samples annealed at 600 °C. For the NT0 series obtained without NaCl, the thickness of the layer increased along with the calcination temperature, whereas for the NT1 series (1 M NaCl during synthesis) the trend is reversed. For NT2 and NT3 series, the thickest films were obtained for NT2_450 and NT3_450 samples.

Synthesis with the addition of 1 M NaCl leads to a decrease in the thickness of the rods. In other words, 1 M NaCl enhances the seeding process, dwindling the growth rate of the crystals. This phenomenon was reported by Sofyan et al., in which the presence of NaCl decreases the size of the particles due to a significant increase in the nucleation rate [47]. The growth rate was affected by the calcination temperature as well. For instance, the synthesis of the NT1 series at 450 °C resulted in rods with two different features, whereas at 300 and 600 °C a uniform rod morphology was observed. Compared to the NT1 series, the NT2 series (2 M NaCl) demonstrated thicker rods revealing proper conditions of crystal growth. Analysis of the morphology of the NT0 to NT3 series revealed that the presence of NaCl during the synthesis process affects the diameter and shapes of the rods, which can be associated with the nucleation reported by Sofyan. The energy-dispersive X-ray spectroscopy (EDS) of the rods indicated the presence of titanium and oxygen, as well as additional signals from FTO glass. No traces of sodium were found in the synthesized samples (see Fig. S6).

More details on the morphology of grown nanorods in the selected samples (NT0_600, NT1_450, NT2_450, NT3_450) were provided by TEM analysis. The SAED patterns collected from the group of nanorods in all samples confirmed the crystallization of the rutile polymorph (Fig. S8, right panels), in agreement with XRD analysis. Nanorods with mainly conical geometry were observed for NT0_600 and NT2_450 (Fig. 4, Fig. S8), while more flat-ended rods were found in NT1_450 and NT3_450. Interestingly, the NT0_600 electrode showed dense single rods, whereas some NT1_450 nanorods (right panel in Fig. 4) were constructed from several single crystal rods (5–15 nm in diameter), growing coherently in the same orientation. This effect is even more pronounced for NT2_450 and NT3_450, where boundaries between thin rods are easily recognizable (Fig. 4), similar to the rods reported previously [32,48–50]. Formation of such aggregates, characterized by larger specific surface areas than single thicker rods, may enhance the adsorption of reactants, which can promote higher photoelectrochemical activity [33,48,49]. Nanorods grew along [001] crystallographic direction ($d_{(001)} = 0.296$ nm) for all samples, while the most exposed planes changed from (110) and (101) (with $d_{(110)} = 0.325$ nm and $d_{(101)} = 0.249$ nm) for NT0_600 and NT1_450 to almost exclusively (110) plane for NT2_450 and NT3_450 (exposed (111) plane was also found on the tip of some nanorod in NT3_450). Additionally, more defects, *e.g.*, folded surface, disordered atom lines, or small disordered domains, were observed for nanorods from NT0_600 and NT1_450 samples. All these observations indicate that the addition of NaCl favors the growth of thinner TiO_2 nanorods (considering diameters of thin single nanorods, not their aggregates) with higher crystallinity and with the exposed (110) crystallographic plane. These results correlate with the previous studies [51–53], as well as with the fact that the (110) plane has the lowest surface energy among other lowest index planes such as (101) [54]. The length of nanorods could not be correctly determined from TEM analysis due to the sample preparation procedure (scraping off nanorod-TiO_2 layer) that resulted in the breaking/shortening of long nanorods/aggregates. Nevertheless, the longest rods were observed for the NT3_450 sample, similar to the conclusions from SEM analysis.

3.3. *Bandgap analysis – diffuse reflectance spectroscopy*

The UV–Vis-DRS spectra are plotted using the Kubelka-Munk function (Fig. S9). According to Fig. S9a, the absorption edge of all electrodes of the NT0 series is placed around 405 nm. The maximum light absorption coefficient in the NT0 series remained comparable for NT0_450 and NT0_600, whereas NT0_300 showed the smaller one, likely due to a lower crystallinity of this sample (compare Fig. 1 and Fig. S1a). The absorption edge of the electrodes in the NT1 series (Fig. S9b) was slightly shifted to the longer wavelengths starting from 410 nm, compared with the NT0 series. The NT1_300 sample showed the smallest absorption coefficient, while NT1_450 and NT1_600 electrodes were characterized by comparable values. Both the NT2 (Fig. S9c) and NT3 (Fig. S9d) series exhibited similar positions of the absorption edge

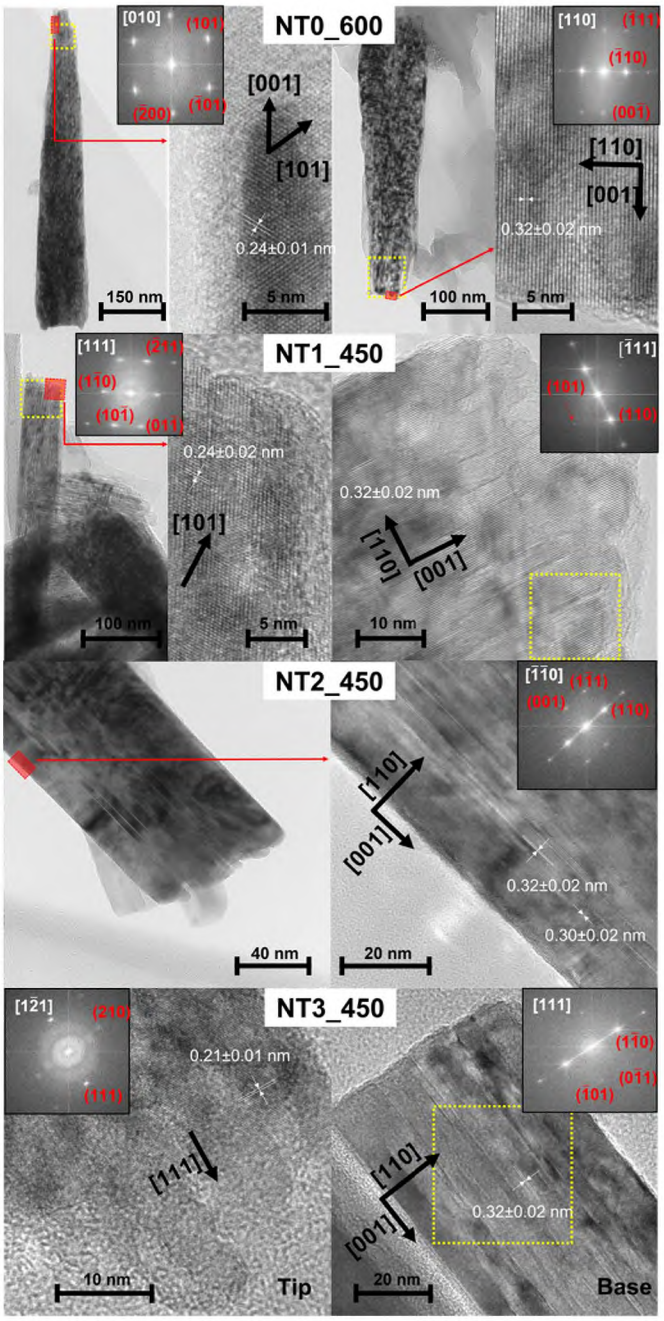

Fig. 4. HR-TEM images of the NT0_600, NT1_450, NT2_450, and NT3_450 electrodes. Inset graphs present a fast Fourier transform (FFT) analysis of the given images, with indexed reflections (red) and zone axis (white). FFT was calculated either for highlighted yellow areas or from the whole image (if no yellow square was shown). (For interpretation of the references to colour in this figure legend, the reader is referred to the Web version of this article.)

located at 410 nm. In general, the absorption coefficient was the highest for the NT2 series. The bandgap energies of the samples were estimated using Tauc plots, and the values are collected in Table S2. The bandgap energies for all the samples are around 3 eV, with the limiting values for NT0 (3.04 eV) and NT2 (2.99 eV) series. The results reveal that the synthesized nanorod-TiO_2 electrodes absorb light in the UV region.

3.4. Photoelectrochemical analysis

3.4.1. PEC analysis under LED light

The photoelectrochemical (PEC) activity of the prepared electrodes was tested by linear sweep voltammetry (LSV) measurements in 0.5 M NaCl under the illumination of LED light ranging within 371–455 nm. The *j-V* curves are shown in Fig. 5a and S15. Since the observed activity trends in each series were analogous for all studied wavelengths (see Fig. 5c), the discussion in the main text is focused on the measurements with the LED of 371 nm – at these conditions, nanorod-TiO_2 electrodes showed the highest PEC activity. The photocurrent density *j* at 1230 mV *vs.* RHE ranges from 2.2 mA cm^{-2} for the NT1_300 electrode to 14.4 mA cm^{-2} for the NT3_450 sample. A gradual increase in photocurrent was observed along with the increase of the calcination temperature within the NT0 series with the highest $j = 6.1$ mA cm^{-2} for the NT0_600 sample (Fig. 5 and Fig. S15). This behavior can be related to the increased crystallinity of the nanorods synthesized at higher temperatures. Interestingly, this trend was changed for samples synthesized in the presence of NaCl – the highest photocurrents were observed for samples annealed at 450 °C, whereas the calcination at 600 °C dwindled the performance of the electrode. This effect seems to be related to the fact that calcination at 450 °C promoted the formation of thicker nanorod-TiO_2 layers compared with annealing at 600 °C (Fig. S7). Independent of calcination temperature, photocurrent density increased along with the rising NaCl concentration used during the synthesis. Accordingly, the NT3 electrodes exhibited a 2–3.4 times higher photocurrent density compared to the respective NT0 samples. These results show the beneficial role of NaCl in enhancing the PEC activity of the electrodes, even those calcined at lower temperatures. The onset potential V_{onset} for the obtained electrodes was in the range of 400–550 mV *vs.* RHE, except for the NT0_300 sample that showed $V_{onset} < 400$ mV. The potential of current saturation was around 700 and 800 mV for the NT0_300 and NT1_300 samples, respectively, whereas the saturation was not reached even at 1600 mV for the other electrodes. The incident photon to current efficiency (IPCE), derived from photocurrent values, is presented in Fig. 5b and Fig. S16. The lowest IPCE of 9 and 13% was observed for NT1_300 and NT0_300 samples, respectively, while the highest activity, among all synthesized samples, was recorded for NT3_450 with IPCE = 57% at 1230 mV *vs.* RHE. The IPCE values at the constant potential of 1000 mV *vs.* RHE were compared in Fig. 5c. The values increased rapidly for wavelength <425 nm (Fig. 5c), which corresponds well to the absorption edge at 410 nm derived from DRS measurements. Since photocurrent density itself does not provide univocal information on the performance of the electrode, the applied bias photon to current efficiency (ABPE), as the main parameter to characterize the activity of photoelectrodes, was calculated according to Eq. (2) (Fig. 5d and Fig. S17):

$$ABPE(\%) = \frac{|j| \times (1.23V - V_{applied})}{P} \quad (2)$$

where *j* is the photocurrent density (mA·cm^{-2}), 1.23 V is the potential of

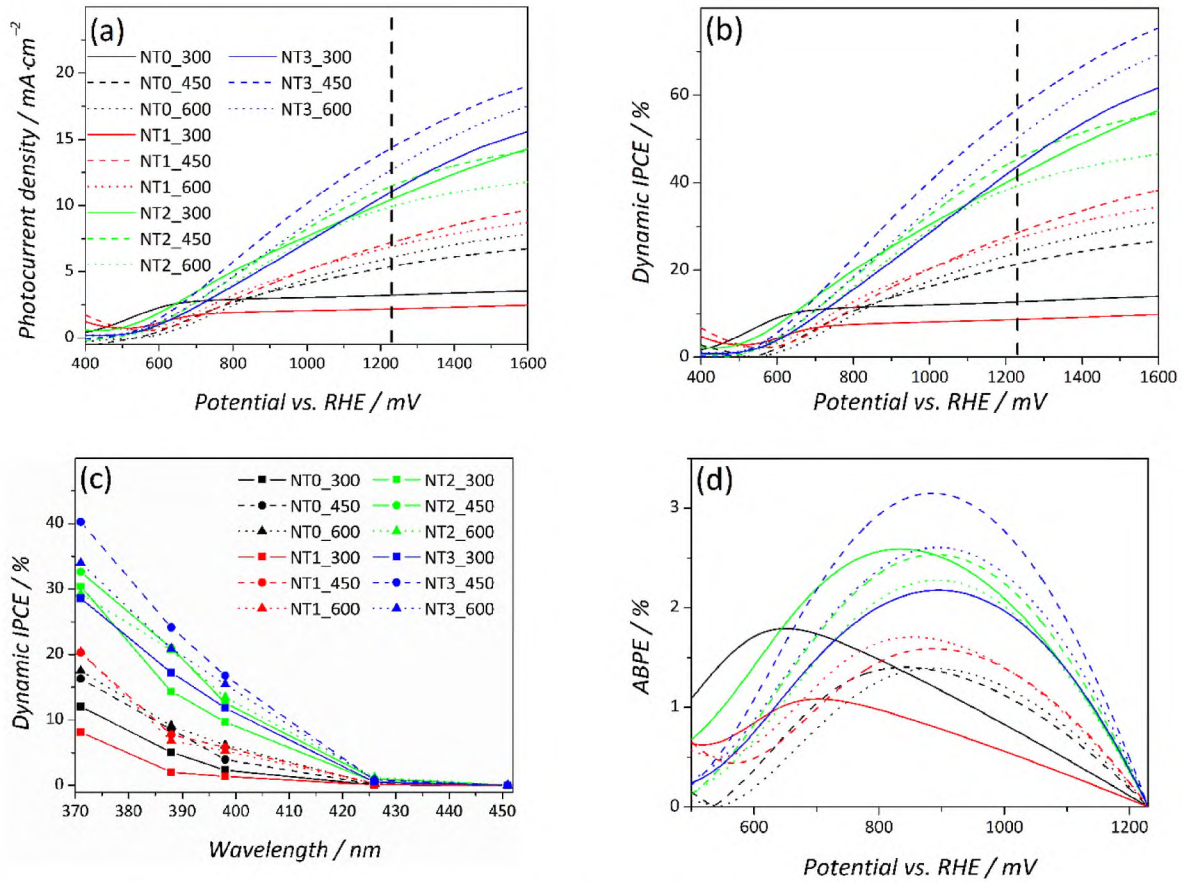

Fig. 5. Parameters derived from linear sweep voltammetry measurements (LSV, scan rate: 10 mV s^{-1}) in 0.5 M NaCl under constant illumination with LED light: photocurrent density for 371 nm (a), incident photon to current efficiency (IPCE) for 371 nm (b), IPCE at 1000 mV *vs.* RHE (c). Applied bias photon to current efficiency (ABPE) for 371 nm (d). Bold vertical lines in (a) and (b) are centered at 1230 mV.

water oxidation, $V_{applied}$ (V) is the potential *versus* RHE applied to the working electrode, and P (mW·cm^{-2}) is the power density of the light. The electrodes demonstrated their highest ABPE values in the range of 800–900 mV (<700 mV for NT0_300 and NT1_300 samples), in which NT3_450 reaches ABPE = 3.15% upon irradiation with 371 nm LED light. Based on these values, we have selected these potentials for further experiments with the solar simulator.

In parallel to the experiments in 0.5 M NaCl discussed above, LSV measurements under LED light were conducted in 0.5 M Na_2SO_4 (Figs. S12–S14). In general, the measured photocurrent densities were lower than those determined in 0.5 M NaCl. The biggest differences under the illumination of 371 nm light were observed for NT0_300 and NT1_300 samples, with five- (0.7 mA cm^{-2}) and four-times (0.5 mA cm^{-2}) lower j at 1230 mV *vs.* RHE in 0.5 M Na_2SO_4. For other electrodes, photocurrent densities differ by maximally 30% with the highest value of 11 mA cm^{-2} at 1230 mV measured for the NT3_450 sample. Consequently, IPCE = 43% at 1230 mV and ABPE = 1.8% at 960 mV for the 371 nm light were determined for NT3_450, which are 14% and 1.35% lower than in 0.5 M NaCl, respectively. These results suggest that the photoelectrochemical activity of nanorod-TiO_2 electrodes with lower crystallinity, as the one synthesized in the NT0 series and NT1_300 sample, is more sensitive to the type of electrolyte used for water-splitting reactions. Interestingly, for the majority of samples, the onset potential was slightly higher (by 50–100 mV) and the slope of the j-V curves was less steep at lower potentials when measured in 0.5 M Na_2SO_4. This may be the consequence of a different mechanism of oxidation reaction at the electrode-electrolyte interface. Moreover, the application of the NaCl electrolyte (optionally seawater) opens the possibility to oxidize not only water but also chloride ions [55]. Also, the improved efficiency of photoelectrochemical reaction in presence of NaCl may be a consequence of the lower activation energy of chloride oxidation compared to water oxidation, and thus more efficient kinetics of this process. The faster kinetics of Cl^- oxidation (owing to the 2e$^-$ process) compared to water oxidation (4e$^-$ process) was already reported by Dresp et al. [55]. In general, in Na_2SO_4, the efficiency of nanorods is lower than in NaCl electrolytes, however, the trend of increasing efficiency is similar. This phenomenon suggests that the increased photocurrent in seawater by 30% (*vide supra*) can be attributed to ClER.

3.4.2. *PEC analysis under solar simulated light (AM 1.5G filter)*

The LSV measurements were also conducted under solar simulated light with AM 1.5G filter for the four top-performing electrodes (with the highest observed photocurrents) from each series: NT0_600, NT1_450, NT2_450, and NT3_450 (Fig. 6a). The highest photocurrent densities in the potential range 400–1600 mV *vs.* RHE were registered for the NT3_450 (0.9 mA cm^{-2} at 1585 mV) and NT2_450 (0.8 mA cm^{-2} at 1575 mV) electrodes, which are more than 2 times higher than those of NT1_450 and NT0_600. Consequently, the NT3_450 sample demonstrated the highest ABPE value of 0.24% at 782 mV (Fig. 6b), which belongs to the highest values reported for pristine TiO_2 nanorods. A comparison of ABPE efficiency with electrodes reported in the literature is given in Table S3. For instance, the ABPE values reported recently ranged from 0.04% [56,57] and 0.1% [58] to 0.22% [27,59]. The performance of the best electrodes reported in this work is also higher than that of TiO_2 nanorods decorated with co-catalysts (*e.g.*, TiO_2@W, and TiO_2@Sn) [58], and similar to the activity of the TiO_2@P–C_3N_4 heterojunction architecture [56,57].

To verify the consistency between experiments with LED light and solar simulator, the ABPE obtained under solar simulated irradiation was re-calculated using the irradiance of the UV region only ($E > 2.99$ eV, $\lambda < 415$ nm; Fig. S19a). The obtained $ABPE_{max}$ of 3.7% and 2.9% for the NT3_450 and NT2_450, respectively, are somewhat higher than the values of 3.15% and 2.5% determined for these samples under 371 nm LED light (the lowest wavelength available with the experimental setup). This result suggests that ABPE at $\lambda < 371$ nm is even higher than the one at 371 nm.

The possible relationship between light intensity and the activity of the nanorod-TiO_2 electrodes was verified by performing LSV scans with the light power ranging from 0.2 to 1.0 Sun for the NT3_450 sample. The photocurrent increased monotonously with the light power (Fig. 7a), whereas ABPE efficiency stayed constant within the experimental accuracy (Fig. 7b). Such observation excludes any influence of light power on the PEC activity within the tested light power range.

3.4.3. *Stability of electrodes under solar simulated light (AM 1.5G filter)*

The PEC stability of the electrodes in seawater oxidation was also studied during 16–20 h of 1 Sun irradiation (4 h irradiation periods with 5 min dark intervals in between) at the applied potential of maximum ABPE (784–810 mV *vs.* RHE). After this period, gas bubbles were removed from the sample cavity in the test cell, the electrolyte was mixed using a magnetic stirrer, and pH was controlled. Then, a short second scan (5 min illumination) was performed (Fig. 8a–d). All samples showed a gradual loss of photocurrent density in the range of 9–19%, after excluding the effect of gas bubbles that accumulated at the semiconductor surface.

The first phase of irradiation (250 min), which is shown in Fig. S20, revealed a 12% photocurrent loss for NT3_450. Upon starting irradiation, a charging spike occurred and was followed by decay for approx. 25 s for NT2_450 and 75 s for NT3_450 (Fig. S20a). Then, NT2_450 showed an increase in photocurrent density for 9–14 min, followed by a gradual decrease, while NT3_450 indicated no increase in the

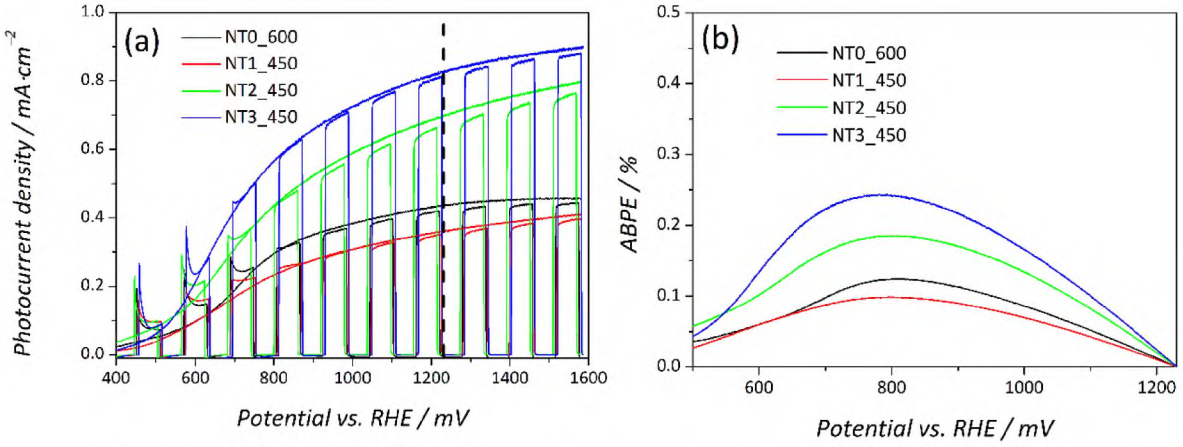

Fig. 6. PEC measurements under constant and modulated 1 Sun illumination in 0.5 M NaCl: LSV data with the scan rate of 10 mV s^{-1} (a), ABPE data (b). The bold vertical line in (a) and is centered at 1230 mV.

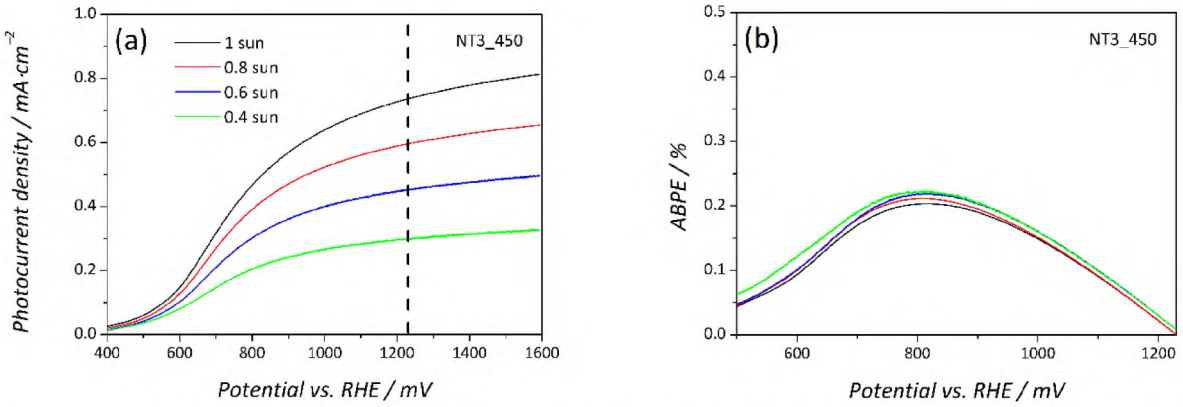

Fig. 7. PEC measurements for the NT3_450 sample in 0.5 M NaCl under simulated solar illumination of different irradiance: LSV data with the scan rate of 10 mV s^{-1} (a), ABPE data (b).

photocurrent density in the first phase (Fig. S20a). In the next illumination intervals, the initial decay times increased to 90–150 s, and no further systematic changes were observed. The decay in the efficiency of the electrodes suggests that the materials undergo a photocorrosion during the long-term (hours-long) measurement. Notably, no qualitative changes were observed in XRD patterns of the optimized samples after PEC measurements (Fig. S2), *i.e.*, corrosion resulted neither from the crystal structure change of nanorods nor the appearance of a new phase. Interestingly, a similar photocorrosion phenomenon was also shown in the work of Iminashi et al., in which the decrease of the photocurrent in a prolonged regime is attributed to the nucleophilic attack of H_2O on the holes trapped at the surface [60]. In addition, Yang et al. showed that photohole-induced corrosion is the key factor in the photocorrosion of TiO_2-nanorod architectures [61]. Thus, to elucidate the photocorrosion occurring in this study and to clarify the role of hole transfer at the semiconductor/electrolyte interface, the measurements employing methanol as a hole scavenger were performed (Fig. 8f) in a time frame of 250 min. In the presence of 5%wt. of methanol, the recorded photocurrents were more stable, with a maximum decrease of <4% for NT3_450 (Fig. 8f), revealing an efficient hole consumption by methanol. Moreover, in methanol, the decay after the initial spike was shorter for NT2_450 (approx. 8 s) and NT3_450 (4 s), while a further increase of photocurrent was much longer, from approx. 20 min for NT3_450 to 4 h for NT0_600 (Fig. 8f and Fig. S20b). This initial spike is attributed to the charge recombination, occurring faster than the methanol or water oxidation at the surface of the electrode. After 4 s (for NT3_450), the charge generation equilibrates with the charge recombination and methanol/water oxidation. An efficient hole consumption by methanol and the mechanism of the photocurrent doubling effect are responsible for the increase and further stabilization of the photocurrent density (Fig. 8f). The ABPE values determined with and without methanol are close to each other for NT3_450 and differ by 10% for NT2_450. The $ABPE_{max}$ recalculated for irradiance from the range of 213–415 nm is equal to 3.8 and 3.3% for NT3_450 and NT2_450, respectively, which are slightly higher values than those measured in 0.5 M NaCl only (Fig. S19).

3.5. Mechanism

3.5.1. Surface photovoltage analysis

Fig. 9 presents the transient surface photovoltage of the nanorod-TiO_2 electrodes. Upon irradiation (380 nm), all samples revealed a drop of the surface photovoltage (SPV) signal, which is related to the accumulation of positive charge at the surface and thus, confirms their n-type conductivity. Among the NT0_series, the largest drop was observed for the NT0_600 sample (338 mV *vs.* 160 mV and 141 mV for NT0_300 and NT0_450, respectively), which indicates the most efficient charge separation. After switching the light off, a moderate rate of relaxation was observed, pointing at the presence of trapping states at the surface, which increases the lifetime of photogenerated charge carriers. These observations correspond with the improved photoelectrochemical activity of the NT0_600 sample in this series.

NT1_300 showed the largest decrease of SPV signal (260 mV) after illumination within the NT1 series, followed by a moderate relaxation of the signal in dark – NT1_450 and NT1_600 show a slightly slower relaxation rate compared to NT1_300. While the lowest SPV signal for NT1_450 (−114 mV) suggests the lowest band bending within this series, the photocurrent measurements indicated the NT1_450 and NT1_600 samples to be far more active compared to NT1_300 (Fig. 5a). This phenomenon suggests the vicinity of an efficient charge process separation and suppressed charge process recombination in these two materials (NT1_450 and NT1_600).

The electrodes from the NT2 series showed a fast evolution of a negative SPV signal ranging from −194 mV to −221 mV. Interestingly, the relaxation rates after switching the light off were extremely slow for these samples, particularly for NT2_450, which can be attributed to the increased concentration of the surface states lowering the rate of the charge recombination. These results are in line with the photocurrent measurements, which indicated NT2_450 to be slightly more active compared to NT2_300 and NT2_600.

In the NT3 series, the most significant negative SPV signal with a moderate declining pace was observed for NT3_450 and NT3_600 electrodes (−287 mV and −280 mV, respectively), much higher than −158 mV for the NT3_300. The latter, however, showed a slower decay of the signal in the dark. Besides NT0_600, the magnitude of SPV for the NT3_450 sample is one of the highest observed for the synthesized nanorod-TiO_2 electrodes. These observations correlate with the photocurrent measurements and highlight the importance of efficient charge separation for reaching the highest photoelectrochemical activity in the NT3_450 electrode.

As thoroughly discussed in our previous paper [26], the SPV signal can offer quantitative insight into the type and number of accumulated charges, as well as the band bending degree upon irradiation. The latter is attributed to the difference between the equilibrated Fermi level and the conduction band of nanorod-TiO_2 [62–64]. The more pronounced band bending can be interpreted as the larger number of positive charges and therefore larger number of active sites at the surface of the electrode. NT3_450 with a slightly lower band bending degree showed two times higher activity compared to NT0_600. This phenomenon is related to the increased charge separation and diminished charge recombination due to the specific morphology of NT3_450, which is constructed from long and thin rods.

3.5.2. Mott-Schottky measurements

To confirm the trend of charge separation and relaxation observed in

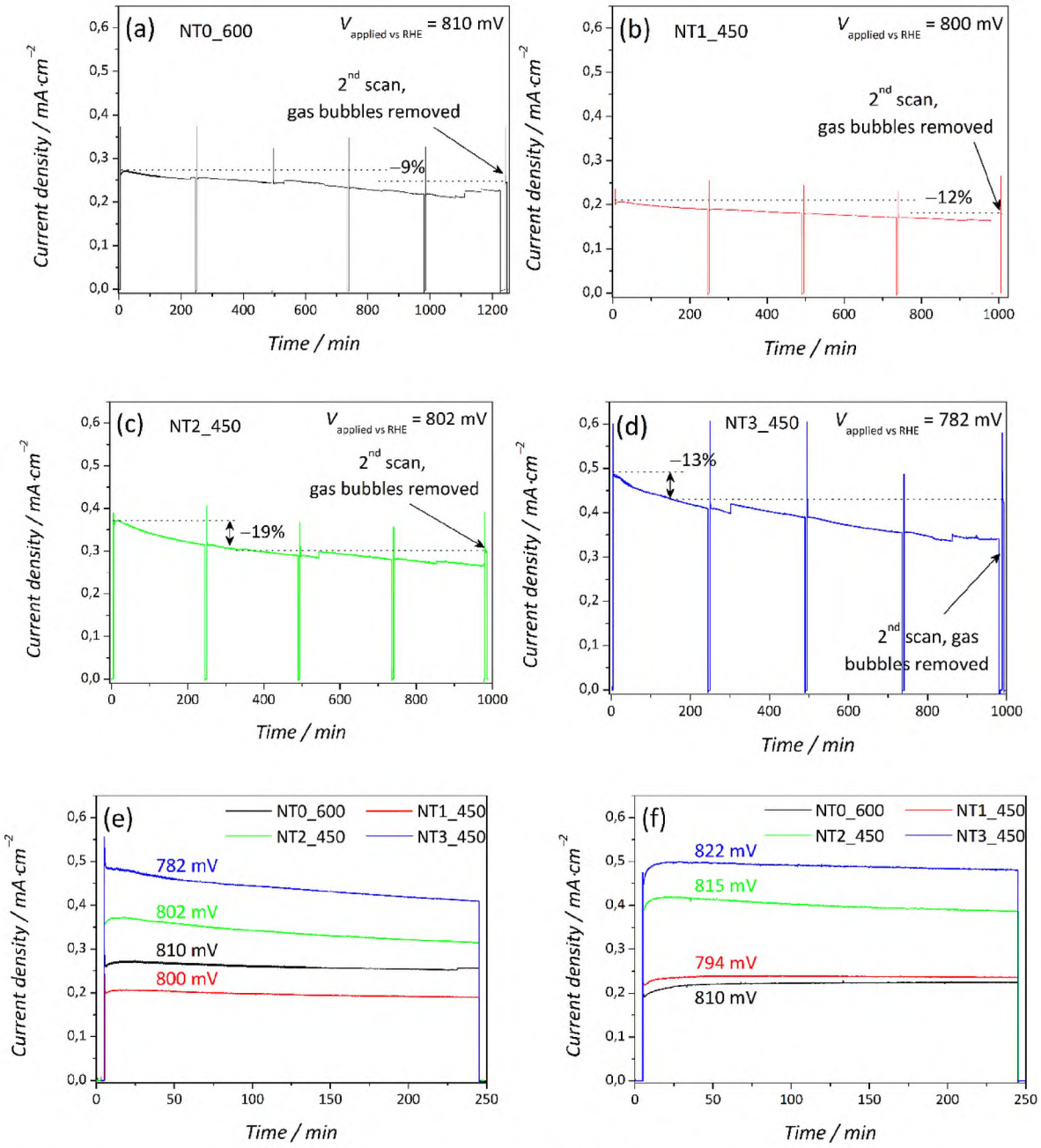

Fig. 8. Chronoamperometric measurements under 1 Sun illumination (ON for 4 h, OFF for 5 min) in 0.5 M NaCl at the potentials of maximum ABPE for NT0_600 (a), NT1_450 (b), NT2_450 (c), and NT3_450 (d) samples. First 4 h-segment of the measurements in 0.5 M NaCl (e). First 4 h segment of the measurements in 0.5 M NaCl +5%wt. methanol as a hole scavenger (f).

SPV, the charge separation and injection yields were calculated according to Dotan et al. [65]. Considering the hole injection yield of the optimized electrodes at the potential of around 800 mV *vs.* RHE (the long-term chronoamperometry measurements were conducted at such potential, Fig. 8), the highest (0.93) and the lowest (0.79) values were determined for NT3_450 and NT0_600 electrodes, respectively (Fig. S21a). Surprisingly, NT1_450 indicated a higher hole injection yield (0.9) compared to NT2_450 (0.82). The trends of charge separation yield, shown in Fig. S21b, corroborate with the total activity (ABPE) of the electrodes. The charge separation yield is ascribed to the number of photogenerated charges, which did not recombine in the bulk and reached the surface, whereas the injection yield is attributed to the number of charges, which are consumed in the reaction without being trapped at the surface. These results are in agreement with the SPV measurements, in which the relaxation times of NT0_600 and NT2_450 are prolonged, pointing at the presence of the trapping states at the surface, which prevents the separated holes from being consumed by the electrolyte.

The Mott-Schottky (M−S) measurements for the most active materials are presented in Fig. S22. The positive slope indicated the *n*-type conductivity of the electrodes, *i.e.*, the accumulation of positive charge carriers at the surface. The observed frequency dispersion is related to the roughness of the surface of the electrodes, which was also reported for TiO_2 by Sivula [66]. However, the roughness should not influence the measurements of the flat band potentials [67]. Therefore, by taking into account the UV-DRS and M−S measurements, the band alignments can be concluded, as shown in Fig. 10. The positions of the band edges are gradually shifted negatively, while the potentials of the VBM in all

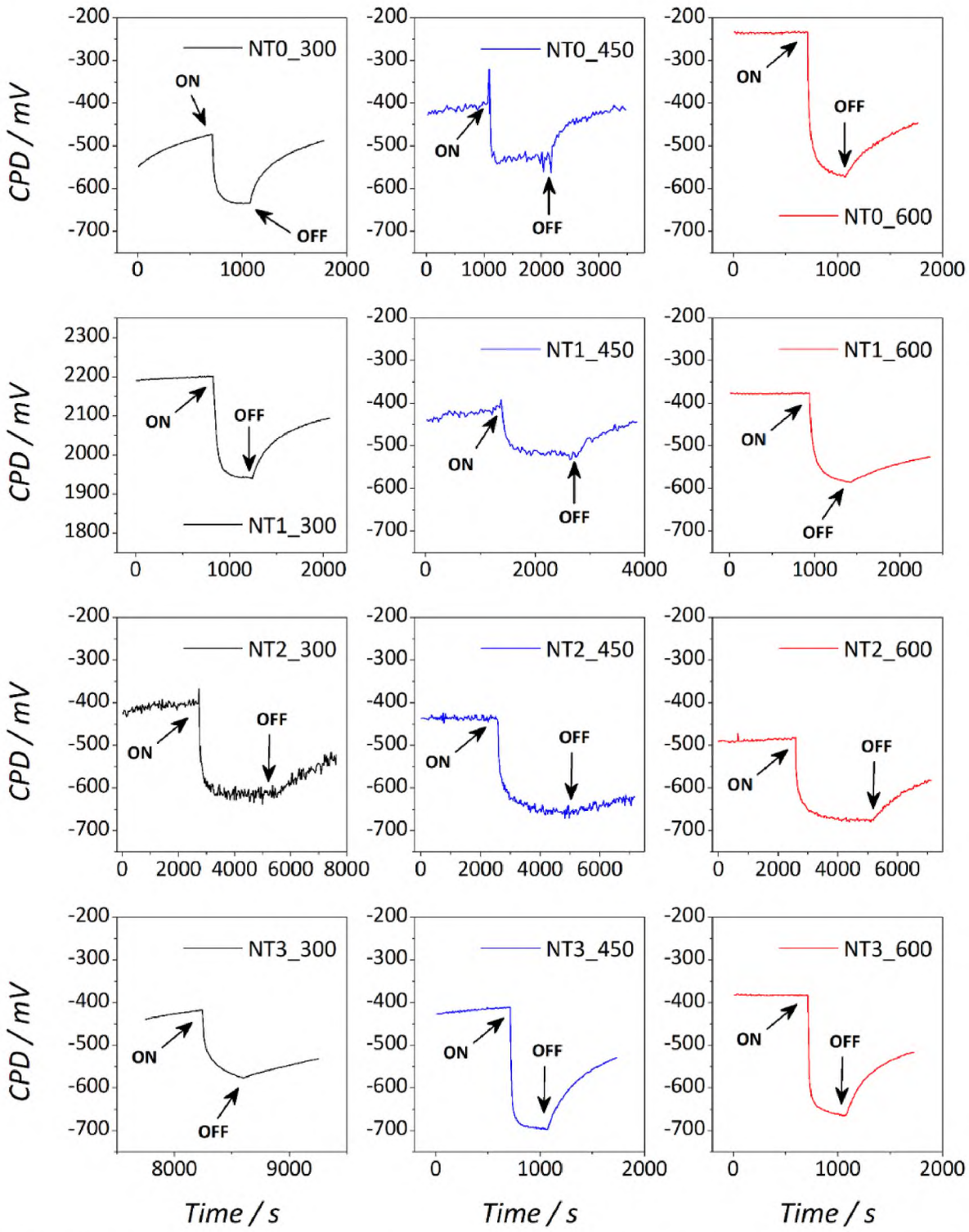

Fig. 9. Surface photovoltage measurements at room temperature, atmospheric conditions, and under illumination with monochromatic light (380 nm).

cases offer appropriate conditions for oxidation of water. In other words, even though the band gap energy has not been influenced by employing NaCl during the synthesis, the positions of band edges were shifted systematically.

3.5.3. *Electrochemical impedance spectroscopy*

The electrochemical impedance spectroscopy (EIS) measurements under simulated solar light and at the OCP (Fig. 11b) showed a general enhancement in the charge transport at the surface of the electrodes compared to the dark (Fig. 11a). In the OCP conditions, there is no current generated in the electrochemical cells and the enhanced conductivity and improved charge transfer under illumination with the simulated solar light are directly attributed to the photo-response of the electrodes. The Nyquist plot of NT3_450, in the dark, showed a semicircle in the high frequencies, which continues with Warburg characteristics at the moderate-low frequencies, indicating the mass transfer between the electrode and electrolyte. The NT1_450 and NT2_450 samples demonstrated identical charge transfer characteristics,

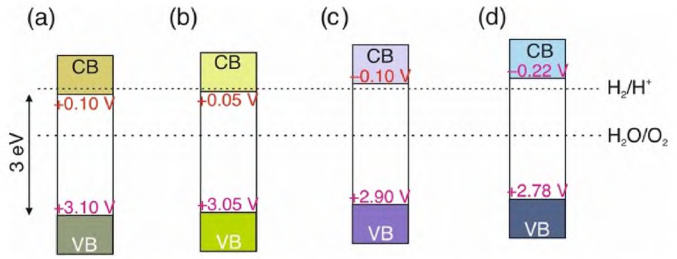

Fig. 10. The band diagram of the most active materials: NT0_600 (a), NT1_450 (b), NT2_450 (c), and NT3_450 (d).

indicating the lowest charge transfer rate at the interface of the electrode/electrolyte. In the dark, NT0_600 indicated the smallest semicircles among all the electrodes. However, the most improved conductivity under irradiation was observed for NT2_450, which also showed the most pronounced change in resistance (Z'') compared to the dark. The spectrum of NT0_600 consisted of three semicircles: the semicircle at low frequencies attributed to charge transfer at the interface of electrode and electrolyte, and semicircles at moderate and high frequencies are ascribed to the diffusion of charge carriers in the bulk. This continues with a Warburg impedance, which indicates depletion of the number of photoelectroactive sites at the surface [68]. Under irradiation, the Nyquist plots of the NT1-NT3 series generally showed two semicircles. The NT1_450 shows the largest semicircles matching the lowest IPCE and ABPE. The NT3_450 is the best-performing electrode, which is matching to the increased conductivity upon irradiation, in parallel to the most efficient charge separation (Fig. 9).

4. Conclusions

The utilization of NaCl during straightforward hydrothermal synthesis plays an important role in the improvement of photoelectrochemical activity of pristine rutile nanorod-TiO_2 electrodes. NaCl facilitates the formation of a thicker TiO_2 layer, composed of aggregates of thinner rods that grow along the [001] direction. It was found that the highest activity in seawater splitting can be reached for electrodes consisting of thicker vertical rods or aggregates of nanorods (major structure) with intergrown thin horizontal rods (minor structure). Although the bandgap energy of nanorod-TiO_2 remained intact for all electrodes upon the increasing concentration of NaCl during the synthesis, the positions of band edges (VB and CB) shifted gradually to the higher energies. Studied electrodes revealed an improvement in the charge transport at the semiconductor/electrolyte interface upon illumination, as deduced from electrochemical impedance spectroscopy. The most beneficial match of structural, morphological, and electronic properties was realized in the NT3_450 sample (3 M NaCl, calcination at 450 °C), which revealed a pronounced increase (by the factor of 2) of the water splitting efficiency compared with NT0_600 electrode synthesized in the absence of NaCl. Moreover, the determined ABPE efficiency of 0.24% under simulated solar irradiation is not only higher than the highest reported values for the pristine nanorod-TiO_2 electrodes but is also similar to the one determined for the TiO_2@P–C_3N_4 heterojunction. Such TiO_2 nanorods obtained through our robust hydrothermal procedure constitute a good starting point for beneficial doping, heterojunction design, or other surface modification aimed to further improve their activity. The TiO_2 nanorods showed a gradual decrease in their performance in long-term exposure to solar light in seawater splitting. The diminished activity is directly related to the inefficient consumption

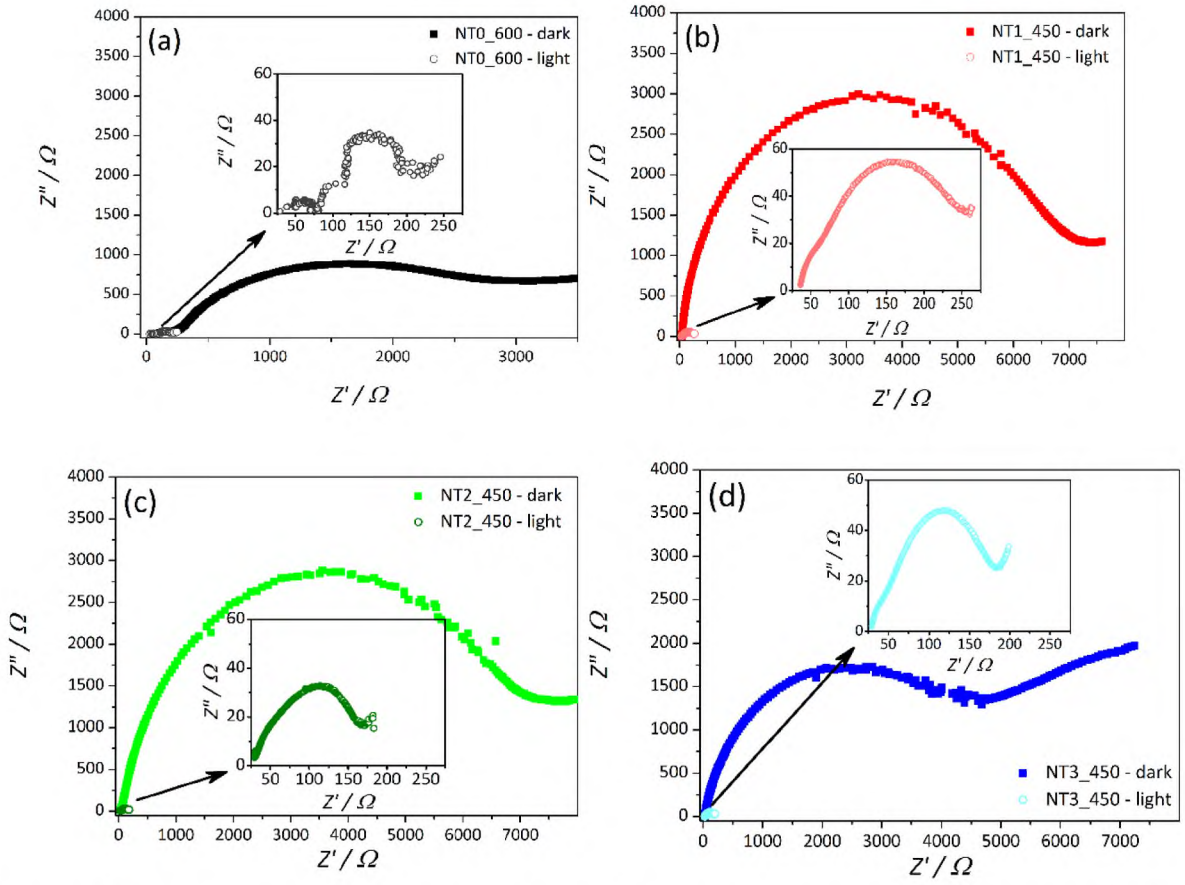

Fig. 11. EIS measurements were conducted in a wide range of frequencies (0.01–10^5 Hz) at the OCP in dark (main figures) and under irradiation with simulated solar light (inset figures) for NT0_600 (a), NT1_450 (b), NT2_450 (c) and NT3_450 (d) samples.

of photogenerated holes, which was resolved by employing methanol as a hole scavenger. Accumulation of holes was also confirmed using surface photovoltage measurements – the NT2_450 electrode showed the highest loss in activity (by 19%), which stems from the presence of trapped holes at the surface. These results point to the significant influence of the synthesis method on the performance of the electrodes. It was also demonstrated that the properties of nanorod-TiO_2 electrodes can be utilized most efficiently by conducting seawater splitting (here 0.5 M NaCl solution) instead of photoelectrolysis of the aqueous solution of Na_2SO_4 – more than 1.5 times higher ABPE at 371 nm was observed for the former process. Compared with Na_2SO_4, the improved efficiency of photons utilization in the presence of NaCl may stem from the lower activation energy of chloride oxidation compared to water oxidation, and hence competition of both reactions during the PEC process. These features of the NaCl solution translate into an improved generation of hydrogen at the cathode.

Credit author statement

Paweł Wyżga: Methodology, Investigation, Writing- Original draft preparation, Visualization. **Taymaz Tabari:** Conceptualization, Methodology, Investigation, Writing- Original draft preparation, Visualization, Supervision. **Mateusz Trochowski:** Formal analysis, Visualization, Writing- Original draft preparation. **Wojciech Macyk:** Conceptualization, Resources, Methodology, Writing- Original draft preparation, Supervision, Project administration, Funding acquisition.

Declaration of competing interest

The authors declare that they have no known competing financial interests or personal relationships that could have appeared to influence the work reported in this paper.

Data availability

Data will be made available on request.

Acknowledgments

The work was supported by the National Science Centre Poland (NCN) within the Solar-Driven Chemistry project (2019/01/Y/ST5/00027) and by National Center for Research and Development (NCBR) within the HERA (Hydrogen Energy Rechargeable Architectures) project (NOR\POLNOR\HERA\0043\2019). The authors gratefully acknowledge Dr. Michał Pacia for SEM analysis, Dr. Marta Gajewska (AGH-UST) for TEM imaging, Dr. Marcin Kobielusz for SPV measurements, and Mrs. Aneta Krasowska for Raman spectroscopy. Our acknowledgments also go to Mrs. Shabnam Jamali for the illustration of the graphical abstract and Dr. Joanna Macyk for the technical and scientific support of the project.

Appendix A. Supplementary data

Supplementary data to this article can be found online at https://doi.org/10.1016/j.rineng.2023.100921.

References

[1] B.J. van Ruijven, E. De Cian, I. Sue Wing, Amplification of future energy demand growth due to climate change, Nat. Commun. 10 (2019) 2762, https://doi.org/10.1038/s41467-019-10399-3.

[2] M.W. Shahzad, M. Burhan, L. Ang, K.C. Ng, Energy-water-environment nexus underpinning future desalination sustainability, Desalination 413 (2017) 52–64, https://doi.org/10.1016/j.desal.2017.03.009.

[3] S. Chu, A. Majumdar, Opportunities and challenges for a sustainable energy future, Nature 488 (2012) 294–303, https://doi.org/10.1038/nature11475.

[4] MdA. Hossen, H.M. Solayman, K.H. Leong, L.C. Sim, N. Yaacof, A. Abd Aziz, L. Wu, M.U. Monir, Recent progress in TiO_2-Based photocatalysts for conversion of CO_2 to hydrocarbon fuels: a systematic review, Results Eng. 16 (2022), 100795, https://doi.org/10.1016/j.rineng.2022.100795.

[5] D.L. McCollum, W. Zhou, C. Bertram, H.-S. de Boer, V. Bosetti, S. Busch, J. Després, L. Drouet, J. Emmerling, M. Fay, O. Fricko, S. Fujimori, M. Gidden, M. Harmsen, D. Huppmann, G. Iyer, V. Krey, E. Kriegler, C. Nicolas, S. Pachauri, S. Parkinson, M. Poblete-Cazenave, P. Rafaj, N. Rao, J. Rozenberg, A. Schmitz, W. Schoepp, D. van Vuuren, K. Riahi, Energy investment needs for fulfilling the Paris agreement and achieving the sustainable development goals, Nat. Energy 3 (2018) 589–599, https://doi.org/10.1038/s41560-018-0179-z.

[6] M. Wang, X. Mao, Y. Xing, J. Lu, P. Song, Z. Liu, Z. Guo, K. Tu, E. Zusman, Breaking down barriers on PV trade will facilitate global carbon mitigation, Nat. Commun. 12 (2021) 6820, https://doi.org/10.1038/s41467-021-26547-7.

[7] K.B. Karnauskas, J.K. Lundquist, L. Zhang, Southward shift of the global wind energy resource under high carbon dioxide emissions, Nat. Geosci. 11 (2018) 38–43, https://doi.org/10.1038/s41561-017-0029-9.

[8] K. Kleiner, Nuclear energy: assessing the emissions, Nat. Clim. Change 1 (2008) 130–131, https://doi.org/10.1038/climate.2008.99.

[9] L. Li, Y. Wang, X. Wang, R. Lin, X. Luo, Z. Liu, K. Zhou, S. Xiong, Q. Bao, G. Chen, Y. Tian, Y. Deng, K. Xiao, J. Wu, M.I. Saidaminov, H. Lin, C.-Q. Ma, Z. Zhao, Y. Wu, L. Zhang, H. Tan, Flexible all-perovskite tandem solar cells approaching 25% efficiency with molecule-bridged hole-selective contact, Nat. Energy (2022), https://doi.org/10.1038/s41560-022-01045-2.

[10] X. Lin, H. Su, S. He, Y. Song, Y. Wang, Z. Qin, Y. Wu, X. Yang, Q. Han, J. Fang, Y. Zhang, H. Segawa, M. Grätzel, L. Han, In situ growth of graphene on both sides of a Cu–Ni alloy electrode for perovskite solar cells with improved stability, Nat. Energy 7 (2022) 520–527, https://doi.org/10.1038/s41560-022-01038-1.

[11] K.O. Brinkmann, T. Becker, F. Zimmermann, C. Kreusel, T. Gahlmann, M. Theisen, T. Haeger, S. Olthof, C. Tückmantel, M. Günster, T. Maschwitz, F. Göbelsmann, C. Koch, D. Hertel, P. Caprioglio, F. Peña-Camargo, L. Perdigón-Toro, A. Al-Ashouri, L. Merten, A. Hinderhofer, L. Gomell, S. Zhang, F. Schreiber, S. Albrecht, K. Meerholz, D. Neher, M. Stolterfoht, T. Riedl, Perovskite–organic tandem solar cells with indium oxide interconnect, Nature 604 (2022) 280–286, https://doi.org/10.1038/s41586-022-04455-0.

[12] B. Abdollahi Nejand, D.B. Ritzer, H. Hu, F. Schackmar, S. Moghadamzadeh, T. Feeney, R. Singh, F. Laufer, R. Schmager, R. Azmi, M. Kaiser, T. Abzieher, S. Gharibzadeh, E. Ahlswede, U. Lemmer, B.S. Richards, U.W. Paetzold, Scalable two-terminal all-perovskite tandem solar modules with a 19.1% efficiency, Nat. Energy (2022), https://doi.org/10.1038/s41560-022-01059-w.

[13] C. Schuschke, C. Hohner, M. Jevric, A. Ugleholdt Petersen, Z. Wang, M. Schwarz, M. Kettner, F. Waidhas, L. Fromm, C.J. Sumby, A. Görling, O. Brummel, K. Moth-Poulsen, J. Libuda, Solar energy storage at an atomically defined organic-oxide hybrid interface, Nat. Commun. 10 (2019) 2384, https://doi.org/10.1038/s41467-019-10263-4.

[14] W.A. Braff, J.M. Mueller, J.E. Trancik, Value of storage technologies for wind and solar energy, Nat. Clim. Change 6 (2016) 964–969, https://doi.org/10.1038/nclimate3045.

[15] D.K. Lee, K.-S. Choi, Enhancing long-term photostability of $BiVO_4$ photoanodes for solar water splitting by tuning electrolyte composition, Nat. Energy 3 (2018) 53–60, https://doi.org/10.1038/s41560-017-0057-0.

[16] H. Wang, Y. Xia, H. Li, X. Wang, Y. Yu, X. Jiao, D. Chen, Highly active deficient ternary sulfide photoanode for photoelectrochemical water splitting, Nat. Commun. 11 (2020) 3078, https://doi.org/10.1038/s41467-020-16800-w.

[17] H. Zhang, W. Tian, J. Zhang, X. Duan, S. Liu, H. Sun, S. Wang, Carbon nitride-based Z-scheme photocatalysts for non-sacrificial overall water splitting, Mater. Today Energy 23 (2022), 100915, https://doi.org/10.1016/j.mtener.2021.100915.

[18] J.N. Hausmann, R. Schlögl, P.W. Menezes, M. Driess, Is direct seawater splitting economically meaningful? Energy Environ. Sci. 14 (2021) 3679–3685, https://doi.org/10.1039/D0EE03659E.

[19] B.A. Pinaud, J.D. Benck, L.C. Seitz, A.J. Forman, Z. Chen, T.G. Deutsch, B.D. James, K.N. Baum, G.N. Baum, S. Ardo, H. Wang, E. Miller, T.F. Jaramillo, Technical and economic feasibility of centralized facilities for solar hydrogen production via photocatalysis and photoelectrochemistry, Energy Environ. Sci. 6 (2013) 1983, https://doi.org/10.1039/c3ee40831k.

[20] J. Bennett, Electrodes for generation of hydrogen and oxygen from seawater, Int. J. Hydrogen Energy 5 (1980) 401–408, https://doi.org/10.1016/0360-3199(80)90021-X.

[21] F. Dionigi, T. Reier, Z. Pawolek, M. Gliech, P. Strasser, Design criteria, operating conditions, and nickel-iron hydroxide catalyst materials for selective seawater electrolysis, ChemSusChem 9 (2016) 962–972, https://doi.org/10.1002/cssc.201501581.

[22] S.-H. Hsu, J. Miao, L. Zhang, J. Gao, H. Wang, H. Tao, S.-F. Hung, A. Vasileff, S. Z. Qiao, B. Liu, An earth-abundant catalyst-based seawater photoelectrolysis system with 17.9% solar-to-hydrogen efficiency, Adv. Mater. 30 (2018), 1707261, https://doi.org/10.1002/adma.201707261.

[23] M. Jadwiszczak, K. Jakubow-Piotrowska, P. Kedzierzawski, K. Bienkowski, J. Augustynski, Highly efficient sunlight-driven seawater splitting in a photoelectrochemical cell with chlorine evolved at nanostructured WO_3 photoanode and hydrogen stored as hydride within metallic cathode, Adv. Energy Mater. 10 (2020), 1903213, https://doi.org/10.1002/aenm.201903213.

[24] Y. Li, Y.-K. Peng, L. Hu, J. Zheng, D. Prabhakaran, S. Wu, T.J. Puchtler, M. Li, K.-Y. Wong, R.A. Taylor, S.C.E. Tsang, Photocatalytic water splitting by N-TiO_2 on MgO (111) with exceptional quantum efficiencies at elevated temperatures, Nat. Commun. 10 (2019) 4421, https://doi.org/10.1038/s41467-019-12385-1.

[25] D. Liu, L. Li, Y. Gao, C. Wang, J. Jiang, Y. Xiong, The nature of photocatalytic "water splitting" on silicon nanowires, Angew. Chem. Int. Ed. 54 (2015) 2980–2985, https://doi.org/10.1002/anie.201411200.

[26] T. Tabari, M. Kobielusz, J. Duch, D. Singh, A. Kotarba, W. Macyk, Design, engineering, and performance of nanorod-Fe_2O_3@rGO@$LaSrFe_{2-n}Co_nO_6$ (n = 0, 1) composite architectures: the role of double oxide perovskites in reaching high solar to hydrogen efficiency, Appl. Catal. B Environ. 272 (2020), 118952, https://doi.org/10.1016/j.apcatb.2020.118952.

[27] F. Ning, M. Shao, S. Xu, Y. Fu, R. Zhang, M. Wei, D.G. Evans, X. Duan, TiO_2/graphene/NiFe-layered double hydroxide nanorod array photoanodes for efficient photoelectrochemical water splitting, Energy Environ. Sci. 9 (2016) 2633–2643, https://doi.org/10.1039/C6EE01092J.

[28] Y. Su, M. Lee, G. Wang, Y. Shih, An innovative method to quickly and simply prepare TiO_2 nanorod arrays and improve their performance in photo water splitting, Chem. Eng. J. 253 (2014) 274–280, https://doi.org/10.1016/j.cej.2014.05.076.

[29] B. Liu, E.S. Aydil, Growth of oriented single-crystalline rutile TiO_2 nanorods on transparent conducting substrates for dye-sensitized solar cells, J. Am. Chem. Soc. 131 (2009) 3985–3990, https://doi.org/10.1021/ja8078972.

[30] Y. Rui, Y. Li, Q. Zhang, H. Wang, Facile synthesis of rutile TiO_2 nanorod microspheres for enhancing light-harvesting of dye-sensitized solar cells, CrystEngComm 15 (2013) 1651, https://doi.org/10.1039/c2ce26691a.

[31] A.H. Jaafar, M.M. Al Chawa, F. Cheng, S.M. Kelly, R. Picos, R. Tetzlaff, N.T. Kemp, Polymer/TiO_2 nanorod nanocomposite optical memristor device, J. Phys. Chem. C 125 (2021) 14965–14973, https://doi.org/10.1021/acs.jpcc.1c02799.

[32] S. Wu, C. Chen, J. Wang, J. Xiao, T. Peng, Controllable preparation of rutile TiO_2 nanorod array for enhanced photovoltaic performance of perovskite solar cells, ACS Appl. Energy Mater. 1 (2018) 1649–1657, https://doi.org/10.1021/acsaem.8b00106.

[33] M. Lv, D. Zheng, M. Ye, J. Xiao, W. Guo, Y. Lai, L. Sun, C. Lin, J. Zuo, Optimized porous rutile TiO_2 nanorod arrays for enhancing the efficiency of dye-sensitized solar cells, Energy Environ. Sci. 6 (2013) 1615, https://doi.org/10.1039/c3ee24125d.

[34] A. Prathan, J. Sanglao, T. Wang, C. Bhoomanee, P. Ruankham, A. Gardchareon, D. Wongratanaphisan, Controlled structure and growth mechanism behind hydrothermal growth of TiO_2 nanorods, Sci. Rep. 10 (2020) 8065, https://doi.org/10.1038/s41598-020-64510-6.

[35] R. Rayathulhan, B.K. Sodipo, A.A. Aziz, Nucleation and growth of zinc oxide nanorods directly on metal wire by sonochemical method, Ultrason. Sonochem. 35 (2017) 270–275, https://doi.org/10.1016/j.ultsonch.2016.10.002.

[36] S. Hazra, V. Tiwari, A. Verma, P. Dolui, A.J. Elias, NaCl as catalyst and water as solvent: highly *E* -selective olefination of methyl substituted *N* -heteroarenes with benzyl amines and alcohols, Org. Lett. 22 (2020) 5496–5501, https://doi.org/10.1021/acs.orglett.0c01851.

[37] S. Hazra, A.K. Kushawaha, D. Yadav, P. Dolui, M. Deb, A.J. Elias, Table salt as a catalyst for the oxidation of aromatic alcohols and amines to acids and imines in aqueous medium: effectively carrying out oxidation reactions in sea water, Green Chem. 21 (2019) 1929–1934, https://doi.org/10.1039/C9GC00497A.

[38] L. Akselrud, Y. Grin, *WinCSD* : software package for crystallographic calculations (Version 4), J. Appl. Crystallogr. 47 (2014) 803–805, https://doi.org/10.1107/S1600576714001058.

[39] P. Makuła, M. Pacia, W. Macyk, How to correctly determine the band gap energy of modified semiconductor photocatalysts based on UV–vis spectra, J. Phys. Chem. Lett. 9 (2018) 6814–6817, https://doi.org/10.1021/acs.jpclett.8b02892.

[40] R. Chen, C. Yang, W. Cai, H.-Y. Wang, J. Miao, L. Zhang, S. Chen, B. Liu, Use of platinum as the counter electrode to study the activity of nonprecious metal catalysts for the hydrogen evolution reaction, ACS Energy Lett. 2 (2017) 1070–1075, https://doi.org/10.1021/acsenergylett.7b00219.

[41] H. Li, X. Shen, Y. Liu, L. Wang, J. Lei, J. Zhang, Facile phase control for hydrothermal synthesis of anatase-rutile TiO_2 with enhanced photocatalytic activity, J. Alloys Compd. 646 (2015) 380–386, https://doi.org/10.1016/j.jallcom.2015.05.145.

[42] O. Frank, M. Zukalova, B. Laskova, J. Kürti, J. Koltai, L. Kavan, Raman spectra of titanium dioxide (anatase, rutile) with identified oxygen isotopes (16, 17, 18), Phys. Chem. Chem. Phys. 14 (2012), 14567, https://doi.org/10.1039/c2cp42763j.

[43] G.C. Vásquez, D. Maestre, A. Cremades, J. Piqueras, Assessment of the Cr doping and size effects on the Raman-active modes of rutile TiO_2 by UV/Visible polarized Raman spectroscopy: assessment of the Cr doping and size effects on the Raman-active modes of rutile TiO_2, J. Raman Spectrosc. 48 (2017) 847–854, https://doi.org/10.1002/jrs.5133.

[44] L. Zhu, Q. Lu, L. Lv, Y. Wang, Y. Hu, Z. Deng, Z. Lou, Y. Hou, F. Teng, Ligand-free rutile and anatase TiO_2 nanocrystals as electron extraction layers for high performance inverted polymer solar cells, RSC Adv. 7 (2017) 20084–20092, https://doi.org/10.1039/C7RA00134G.

[45] Z. Jiang, W. Zhang, L. Jin, X. Yang, F. Xu, J. Zhu, W. Huang, Direct XPS evidence for charge transfer from a reduced rutile TiO_2 (110) surface to Au clusters, J. Phys. Chem. C 111 (2007) 12434–12439, https://doi.org/10.1021/jp073446b.

[46] I. Ibrahim, G.V. Belessiotis, M. Antoniadou, A. Kaltzoglou, E. Sakellis, F. Katsaros, L. Sygellou, M.K. Arfanis, T.M. Salama, P. Falaras, Silver decorated TiO_2/g-C_3N_4 bifunctional nanocomposites for photocatalytic elimination of water pollutants under UV and artificial solar light, Results Eng. 14 (2022), 100470, https://doi.org/10.1016/j.rineng.2022.100470.

[47] N. Sofyan, A. Ridhova, A.H. Yuwono, M.C. Sianturi, Effect of NaCl addition on nano rosette TiO_2 crystal growth during hydrothermal deposition, IJTech 10 (2019) 1235, https://doi.org/10.14716/ijtech.v10i6.3630.

[48] W. Guo, C. Xu, X. Wang, S. Wang, C. Pan, C. Lin, Z.L. Wang, Rectangular bunched rutile TiO_2 nanorod arrays grown on carbon fiber for dye-sensitized solar cells, J. Am. Chem. Soc. 134 (2012) 4437–4441, https://doi.org/10.1021/ja2120585.

[49] M. Lv, D. Zheng, M. Ye, L. Sun, J. Xiao, W. Guo, C. Lin, Densely aligned rutile TiO_2 nanorod arrays with high surface area for efficient dye-sensitized solar cells, Nanoscale 4 (2012) 5872, https://doi.org/10.1039/c2nr31431b.

[50] H. Zhang, X. Liu, Y. Li, Q. Sun, Y. Wang, B.J. Wood, P. Liu, D. Yang, H. Zhao, Vertically aligned nanorod-like rutileTiO_2 single crystal nanowire bundles with superior electron transport and photoelectrocatalytic properties, J. Mater. Chem. 22 (2012) 2465–2472, https://doi.org/10.1039/C2JM15546J.

[51] A. Prathan, J. Sanglao, T. Wang, C. Bhoomanee, P. Ruankham, A. Gardchareon, D. Wongratanaphisan, Controlled structure and growth mechanism behind hydrothermal growth of TiO_2 nanorods, Sci. Rep. 10 (2020) 8065, https://doi.org/10.1038/s41598-020-64510-6.

[52] E. Hosono, S. Fujihara, K. Kakiuchi, H. Imai, Growth of submicrometer-scale rectangular parallelepiped rutile TiO_2 films in aqueous $TiCl_3$ solutions under hydrothermal conditions, J. Am. Chem. Soc. 126 (2004) 7790–7791, https://doi.org/10.1021/ja048820p.

[53] E. Bae, N. Murakami, T. Ohno, Exposed crystal surface-controlled TiO_2 nanorods having rutile phase from $TiCl_3$ under hydrothermal conditions, J. Mol. Catal. Chem. 300 (2009) 72–79, https://doi.org/10.1016/j.molcata.2008.10.048.

[54] U. Diebold, The surface science of titanium dioxide, Surf. Sci. Rep. 48 (2003) 53–229, https://doi.org/10.1016/S0167-5729(02)00100-0.

[55] S. Dresp, F. Dionigi, M. Klingenhof, P. Strasser, Direct electrolytic splitting of seawater: opportunities and challenges, ACS Energy Lett. 4 (2019) 933–942, https://doi.org/10.1021/acsenergylett.9b00220.

[56] Z. Liang, H. Hou, Z. Fang, F. Gao, L. Wang, D. Chen, W. Yang, Hydrogenated TiO_2 nanorod arrays decorated with carbon quantum dots toward efficient photoelectrochemical water splitting, ACS Appl. Mater. Interfaces 11 (2019) 19167–19175, https://doi.org/10.1021/acsami.9b04059.

[57] Z. Yu, Y. Li, J. Qu, R. Zheng, J.M. Cairney, J. Zhang, M. Zhu, A. Khan, W. Li, Enhanced photoelectrochemical water-splitting performance with a hierarchical heterostructure: Co_3O_4 nanodots anchored TiO_2@P-C_3N_4 core-shell nanorod arrays, Chem. Eng. J. 404 (2021), 126458, https://doi.org/10.1016/j.cej.2020.126458.

[58] B. Chen, B. Ge, S. Fu, Q. Li, X. Chen, L. Li, J. Wang, Z. Yang, J. Ding, W. Fan, B. Mao, W. Shi, Ex-situ flame co-doping of tin and tungsten ions in TiO_2 nanorod arrays for synergistic promotion of solar water splitting, Chem. Eng. Sci. 226 (2020), 115843, https://doi.org/10.1016/j.ces.2020.115843.

[59] P. Wen, F. Su, H. Li, Y. Sun, Z. Liang, W. Liang, J. Zhang, W. Qin, S.M. Geyer, Y. Qiu, L. Jiang, A Ni_2P nanocrystal cocatalyst enhanced TiO_2 photoanode towards highly efficient photoelectrochemical water splitting, Chem. Eng. J. 385 (2020), 123878, https://doi.org/10.1016/j.cej.2019.123878.

[60] A. Imanishi, T. Okamura, N. Ohashi, R. Nakamura, Y. Nakato, Mechanism of water photooxidation reaction at atomically flat TiO_2 (rutile) (110) and (100) surfaces: dependence on solution pH, J. Am. Chem. Soc. 129 (2007) 11569–11578, https://doi.org/10.1021/ja073206+.

[61] Y. Yang, Y. Ling, G. Wang, T. Liu, F. Wang, T. Zhai, Y. Tong, Y. Li, Photohole induced corrosion of titanium dioxide: mechanism and solutions, Nano Lett. 15 (2015) 7051–7057, https://doi.org/10.1021/acs.nanolett.5b03114.

[62] T. Dittrich, S. Fengler, N. Nickel, Surface photovoltage spectroscopy over wide time domains for semiconductors with ultrawide bandgap: example of gallium oxide, Phys. Status Solidi A 218 (2021), 2100167, https://doi.org/10.1002/pssa.202100167.

[63] V. Donchev, Surface photovoltage spectroscopy of semiconductor materials for optoelectronic applications, Mater. Res. Express 6 (2019), 103001, https://doi.org/10.1088/2053-1591/ab3bf0.

[64] K.-H. Ye, H. Li, D. Huang, S. Xiao, W. Qiu, M. Li, Y. Hu, W. Mai, H. Ji, S. Yang, Enhancing photoelectrochemical water splitting by combining work function tuning and heterojunction engineering, Nat. Commun. 10 (2019) 3687, https://doi.org/10.1038/s41467-019-11586-y.

[65] H. Dotan, K. Sivula, M. Grätzel, A. Rothschild, S.C. Warren, Probing the photoelectrochemical properties of hematite (α-Fe_2O_3) electrodes using hydrogen peroxide as a hole scavenger, Energy Environ. Sci. 4 (2011) 958–964, https://doi.org/10.1039/C0EE00570C.

[66] K. Sivula, Mott–Schottky analysis of photoelectrodes: sanity checks are needed, ACS Energy Lett. 6 (2021) 2549–2551, https://doi.org/10.1021/acsenergylett.1c01245.

[67] A. Hankin, F.E. Bedoya-Lora, J.C. Alexander, A. Regoutz, G.H. Kelsall, Flat band potential determination: avoiding the pitfalls, J. Mater. Chem. A. 7 (2019) 26162–26176, https://doi.org/10.1039/C9TA09569A.

[68] A.R.C. Bredar, A.L. Chown, A.R. Burton, B.H. Farnum, Electrochemical impedance spectroscopy of metal oxide electrodes for energy applications, ACS Appl. Energy Mater. 3 (2020) 66–98, https://doi.org/10.1021/acsaem.9b01965.